ACS APPLIED MATERIALS & INTERFACES

Research Article

www.acsami.org

Self-Assembled Amphiphilic Block Copolymers/CdTe Nanocrystals for Efficient Aqueous-Processed Hybrid Solar Cells

Jun-Huan Li,[†,‡] Yilin Li,[‡] Jun-Ting Xu,[*,†] and Christine K. Luscombe[*,‡,§]

[†]MOE Key Laboratory of Macromolecular Synthesis and Functionalization, Department of Polymer Science & Engineering, Zhejiang University, Hangzhou 310027, China

[‡]Materials Science & Engineering Department, University of Washington, Seattle, Washington 98195-2120, United States

[§]Department of Chemistry, University of Washington, Seattle, Washington 98195-1700, United States

Supporting Information

ABSTRACT: Due to their low cost and high efficiency, polymer/nanocrystal hybrid solar cells (HSCs) have attracted much attention in recent years. In this work, water-soluble hybrid materials consisting of amphiphilic block copolymers (ABCPs) and cadmium telluride nanocrystals (CdTe NCs) were used as the active layer to fabricate the HSCs via aqueous processing. The ABCPs composed of poly(3-hexylthiophene) (P3HT) and poly(acrylic acid) (PAA) self-assembled into ordered nanostructured micelles which then transformed to nanowires by comicellization with P3HT additives. Furthermore, after annealing, the hybrid materials formed an interpenetrating network which resulted in a maximum power conversion efficiency of 4.8% in the HSCs. The properties of the hybrid materials and the film morphology were studied and correlated to the device performance. The results illustrate how the inclusion of ABCPs for directed assembly and homo-P3HT for charge transport and light absorption improves device performance. The aqueous-processed HSCs based on the ABCPs and NCs offer an effective method for the fabrication of efficient solar cells.

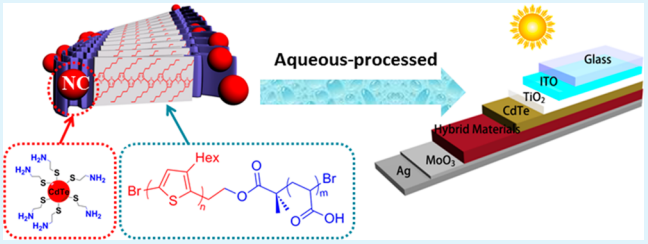

KEYWORDS: *self-assembled, amphiphilic block copolymer, aqueous-processed, hybrid, solar cells*

1. INTRODUCTION

Aqueous-processed solar cells have attracted much interest recently because they exhibit the potential to produce clean energy via the use of nontoxic solvents.[1−3] The use of water instead of toxic organic solvents during the fabrication process of these devices is capable of significantly reducing the environmental impact as well as the production cost. In aqueous-processed solar cells, hybrid solar cells (HSCs) employing water-soluble conjugated polymers (WCPs) and inorganic nanocrystals (NCs) as photovoltaic materials have gained much attention.[4−6] These hybrid materials take advantage of both WCPs and NCs, which exhibit adjustable absorption properties through structural modification,[7,8] efficient charge carrier generation,[9,10] and high charge carrier mobility.[11]

WCPs are typically homopolymers with ionic (i.e., sulfonate and phosphonate moieties) or nonionic, hydrophilic (i.e., hydroxyl and glycol moieties) side chains. Manca et al. reported the use of water-soluble derivatives of polythiophene conjugated with alkanoate side chains as the electron donor and TiO_2 nanoparticles as the electron acceptor in devices, which attained a power conversion efficiency (PCE) of 0.7%.[12] Unfortunately, the use of hydrophilic side chains in these conventional WCPs adversely affected the stacking of the polymer backbone, which led to the deterioration of their optoelectronic properties (i.e., carrier transport and charge dynamics) and thus a lower PCE of their HSCs.[13] Furthermore, these side chains may cause charge trapping when applied in the active layer, which results in the further reduction in performance.[14,15]

Thermal annealing is an effective method to remove the side groups after film formation, thereby providing a pathway toward improving polymer stacking and thus their optoelectronic properties. To this end, Yang et al. introduced CdTe NCs as the acceptor and water-soluble π-conjugated polymer precursors as the donor, followed by a thermal annealing step.[6,16,17] These CdTe NCs/polymer precursor-based HSCs exhibited PCEs up to 4.76% via optimized thermal annealing of the active layer.[16] However, this method requires a long annealing process (at least 1 h), which is energy intensive, and it also requires thermally cleavable side groups (i.e., thiophenium moieties), limiting the types of polymer precursors that can be used.

Another approach to incorporating π-conjugated, hydrophobic polymers into devices using water as a solvent is to create aqueous nanoparticle dispersions containing the π-conjugated polymer.[18−20] For example, Kietzke et al.[19] and Andersen et al.[18] mixed small molecule surfactants with the π-

Received: March 2, 2017
Accepted: May 9, 2017
Published: May 9, 2017

DOI: 10.1021/acsami.7b03074
ACS Appl. Mater. Interfaces 2017, 9, 17942−17948

conjugated polymer to create the aqueous nanoparticle dispersions. More recently, Yao et al. created the dispersions using amphiphilic block copolymers (ABCPs).[20] ABCPs have been applied in various areas such as biomedical drug delivery,[21] sensing and imaging,[22] nanophotonics,[23] and preparation of nanostructured materials.[24−26] Due to the chemically distinct polymeric segments that are joined together covalently, ABCPs can self-assemble into ordered structures, which allows for improved morphological control[20] when compared to the surfactant containing nanoparticle dispersions.[18,19] Furthermore, modification of the interior or the exterior of the ABCP assemblies can be achieved by either using different polymer blocks[24,27] or by introducing additives.[27−29] For example, recent studies have shown that the introduction of homopolymers as chemical additives can be effective in manipulating the nanostructure and properties of ABCP assemblies either by acting as a glue to create extended cylindrical micelles[30] or converting spherical micelles into platelets.[31,32]

To this end, Yao et al. created aqueous polymer dots by mixing a block copolymer poly(styrene-*co*-maleic anhydride) (PSMA) with P3HT under sonication in water.[20] During this process, the maleic anhydride hydrolyzed in water, thus converting PSMA into an ABCP. The P3HT chains and the polystyrene formed the core of the polymer dots. These polymer dots were then mixed with CdTe NCs to fabricate HSCs using aqueous solution processing. The optimized CdTe NCs/polymer dot HSCs showed a 4.12% PCE. However, due to the insulating nature of PSMA, the polymer dots used in this system had unfavorable optoelectronic properties (i.e., light absorption and charge carrier mobility). To address these issues, one possible solution is to use ABCPs containing a semiconducting π-conjugated polymer block.

In this study, a π-conjugated polymer containing ABCP, specifically a P3HT-containing ABCP, was synthesized and used to fabricate HSCs. The ABCPs containing the semiconducting P3HT chains self-assembled into spherical and cylindrical micelles in water, which were further transformed into nanowires by the introduction of homo-P3HT additives. The nanowire-like features acted as a template to assemble CdTe NCs and affected the resulting film morphology within a short annealing time (15 min). The HSCs fabricated by using the hybrid material consisting of the ABCP, homo-P3HT, and CdTe NCs showed a PCE of 4.8% for the best performing device. The properties of the hybrid materials and the film morphology were studied and correlated to the device performance. The combination of π-conjugated polymer containing ABCPs and NCs provides a facile and feasible protocol to fabricate efficient HSCs.

2. RESULTS AND DISCUSSION

2.1. Synthesis of Hybrid Materials. Two hybrid materials were synthesized in this study. CdTe NCs were used as the inorganic portion for both hybrid materials, while two different micelles were used as the organic portion. One micelle is the ABCP-only micelle, which was assembled from a poly(3-hexylthiophene)-*block*-poly(acrylic acid) ($P3HT_{25}$-*b*-PAA_{73}), where the subscripts indicate the number of repeat units in each block. The other is the ABCP and homopolymer comicelle, which was assembled from the aforementioned ABCP with $P3HT_{11}$. We refer to the hybrid ABCP micelle/CdTe and the hybrid ABCP/P3HT micelle/CdTe as block copolymer (BCP) hybrids and block copolymer/homopolymer (BH) hybrids, respectively. The synthesis of the ABCP is depicted in Scheme 1. Briefly, vinyl-terminated $P3HT_{25}$ (^{1}H NMR in Figure S1) was synthesized via Kumada catalyst-transfer polymerization (KCTP).[33] Hydroxyl-terminated $P3HT_{25}$ (^{1}H NMR in Figure S2) was synthesized via hydroboration−oxidation reaction from vinyl-terminated $P3HT_{25}$ and was further converted into bromoester-terminated $P3HT_{25}$ (^{1}H NMR in Figure S3) by reacting with α-bromoisobutyryl bromide. The bromoester-terminated $P3HT_{25}$ was used as macroinitiator for atom transfer radical polymerization (ATRP) of *tert*-butyl acrylate, resulting in the formation of $P3HT_{25}$-*b*-$PtBA_{73}$ (^{1}H NMR in Figure S4). $P3HT_{25}$-*b*-PAA_{73} was obtained by removing the *tert*-butyl group from $P3HT_{25}$-*b*-$PtBA_{73}$ in the presence of trifluoroacetic acid. The water-soluble CdTe NCs (Scheme 2b and Figure S8) were synthesized by adding NaHTe solution into the precursor containing Cd^{2+} and mercaptoethylamine, which was further refluxed for the growth of NCs under nitrogen.[2]

Scheme 1. Synthesis of Poly(3-hexylthiophene)-*block*-poly(acrylic acid) (P3HT-*b*-PAA)

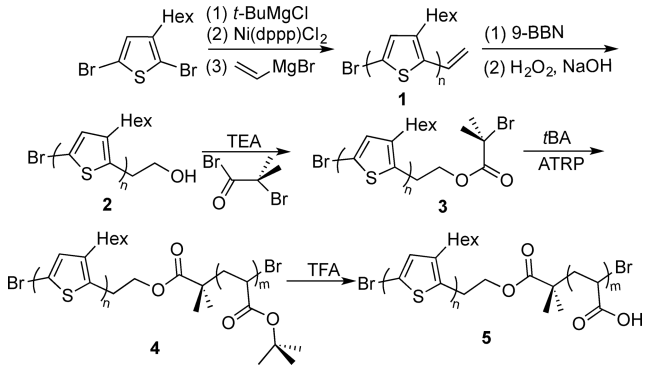

Scheme 2. Schematic Structures of (a) BCP Micelle, BH Micelle, and (b) CdTe NCs

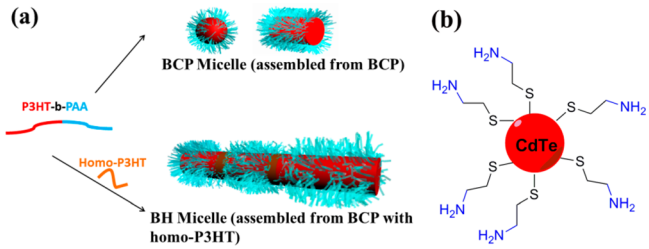

2.2. Characterizations of Micelles and Hybrid Materials. Figure 1a is the transmission electron microscopy (TEM) image of the BCP micelles in aqueous solution. The formation of BCP micelles in aqueous solution is driven by the aggregation of the hydrophobic $P3HT_{25}$ segment. This is confirmed by the significant red-shift (Figure 1c) of the main absorption peak of the BCP micelle in water (λ_{max} = 510 nm) compared to that of the ABCP in THF (λ_{max} = 446 nm) and the appearance of the vibronic features at 545 and 600 nm.[34] It is noted that the BCP micelles are spherical and cylindrical in shape (Figure 1a and Scheme 2a). The bimodal size distribution observed in the dynamic light scattering (DLS) data (Figure S9) is in agreement with the TEM images. The formation of mixed-shaped micelles may be due to the micelles becoming kinetically trapped because of their inability to

DOI: 10.1021/acsami.7b03074
ACS Appl. Mater. Interfaces 2017, 9, 17942−17948

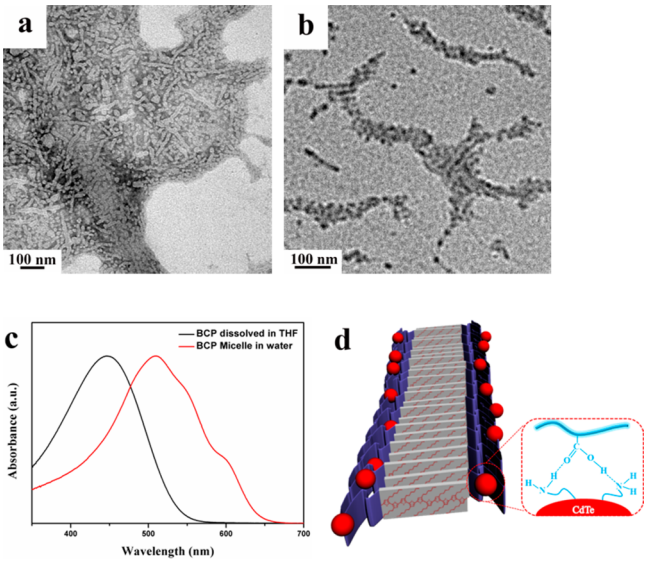

Figure 1. TEM images of (a) BCP micelles (stained with phosphotungstic acid to increase the color contrast between the micelle core and the background for better visibility) and (b) BCP hybrid. The darker spheres in panel b correspond to NCs. (c) Normalized UV−vis spectra of BCP dissolved in THF and semicrystalline BCP micelle in water. (d) Schematic diagram of the BCP hybrid.

thermodynamically equilibrate to form homogeneous, spherical structures.[35,36] The slow diffusion kinetics of BCPs in solution, caused by the lack of chain exchange between micelles due to the high molecular weight of the molecules and repulsion effects of water on the core block (P3HT), may hinder assembled structures from reaching a global equilibrium and may provide the mixed-shape micelles.

Figure 1b shows the TEM image after the addition of CdTe NCs to the BCP micelles to form the BCP hybrid. It can be seen that the CdTe NCs (black dots in Figure 1b) are primarily localized in the same area as the BCP micelles (dark gray regions). We attribute this to the hydrogen bonding interaction that can take place between the amine-terminated ligands on the CdTe NCs and COOH groups on the exterior of the BCP micelles (schematically represented in Figure 1d) as confirmed by Fourier transform infrared (FTIR) spectroscopy (Figure S10).

Figure 2a depicts the TEM image of BH micelles in aqueous solution. It was found that the morphology of BH micelles was

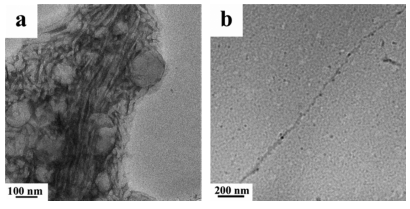

Figure 2. TEM images of (a) BH micelles (stained with phosphotungstic acid) and (b) BH hybrid.

notably different from the BCP micelles; specifically, long nanowires could be observed. The transition of bimodal to unimodal distribution and the shift of the overall micellar size were clearly seen in DLS (Figure S9), which agree with the morphological transformation seen in the TEM images. In BH micelles, the low molecular weight homopolymer $P3HT_{11}$ can interpenetrate into the $P3HT_{25}$ core of the BCP micelles, which increases the separation between the PAA chains in the exterior of the micelle. This then allows the spheres or cylinders to convert to longer nanowires.[28,37] It is also noted that circular features are visible in Figure 2a. These arose because the samples were prepared from freeze-drying in liquid nitrogen to maintain the original state of the micelles in solution. Bubbles existed due to the sample preparation under vacuum and resulted in the seemingly round-shape large particles.[38] The unimodal distribution observed through DLS (Figure S9) also supports that large particles are absent prior to TEM sample preparation. For the BH hybrid, Figure 2b shows that the CdTe NCs tend to distribute along the BH micelles to form high aspect ratio linear structures. Similarly to the BCP hybrid, the hydrogen-bonding interaction between NCs and polymers likely facilitates the compatibility of both materials in the film state.[39]

2.3. Device Performance of Hybrid Materials. The performance of these hybrid materials for solar cell application was studied by fabricating complete photovoltaic devices. The device structure is presented in Figure 3a along with the energy

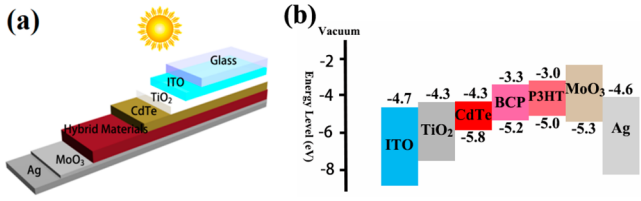

Figure 3. (a) Device structure and (b) energy level diagram. ITO, TiO_2, MoO_3, and Ag refer to indium tin oxide, titanium dioxide, molybdenum trioxide, and silver, respectively.

level diagram (Figure 3b), where TiO_2 and MoO_3 were used as the electron transport layer and hole transport layer, respectively. The energy levels of the CdTe NCs, BCP, and $P3HT_{11}$ were obtained using ultraviolet photoelectron spectroscopy (UPS) (Figure S11), while the energy levels of ITO, TiO_2, MoO_3, and Ag were extracted from the literature.[20,40] A pure CdTe NC layer in the device was introduced to enhance the light absorption and electron selectivity.[16] Hybrid materials containing micelles and NCs were applied to form the active layer. A device using pure CdTe NCs was also fabricated for comparison. The related device performance, including short-circuit current density (J_{sc}), open circuit voltage (V_{oc}), fill factor (FF), PCE, the shunt resistance (R_{sh}), the series resistance (R_s), and film thickness are listed in Table 1 and depicted in Figure 4a.

Table 1 shows that the introduction of BCP improves all of the device parameters compared to CdTe NC solar cells. Under the optimized conditions (Table S3−S6), the performance of the BCP hybrid device showed improved average PCEs from 2.79 to 4.13%. When the BH hybrid was applied as the active material, the solar cell devices exhibited an average efficiency of 4.76%.

The increase in J_{sc} after introducing polymers into the CdTe NCs was further confirmed by the EQE of the devices (Figure 4b). It was found that the EQE of the devices prepared with the BCP hybrid improved compared to those with pure CdTe NCs, especially in the range of 400−650 nm. The EQE of the BH hybrid containing devices increased even further, which is in accordance with the increase in J_{sc}. The J_{sc} values based on

DOI: 10.1021/acsami.7b03074
ACS Appl. Mater. Interfaces 2017, 9, 17942−17948

Table 1. Device Performance Parameters with Pure CdTe NCs, the BCP Hybrid, or BH Hybrid as Active Materials[a]

composition	J_{sc} (mA/cm^2)	V_{oc} (mV)	FF (%)	PCE (%)	R_{sh} ($\times 10^3$ Ω·cm^2)	R_s (Ω·cm^2)	T[b] (nm)
CdTe NCs	13.9 ± 0.3	467 ± 6	42.8 ± 0.6	2.79 ± 0.05	2.32 ± 0.11	11.1 ± 0.5	102 ± 9
BCP hybrid	15.3 ± 0.2	529 ± 3	51.2 ± 0.3	4.13 ± 0.05	3.12 ± 0.10	8.4 ± 0.3	105 ± 6
BH hybrid	16.2 ± 0.3	543 ± 5	54.1 ± 0.4	4.76 ± 0.09	3.93 ± 0.13	5.8 ± 0.3	107 ± 7

[a]Data are averaged over at least five devices and presented as mean ± standard deviation. [b]T represents the active layer thickness excluding the first pure CdTe NC layer.

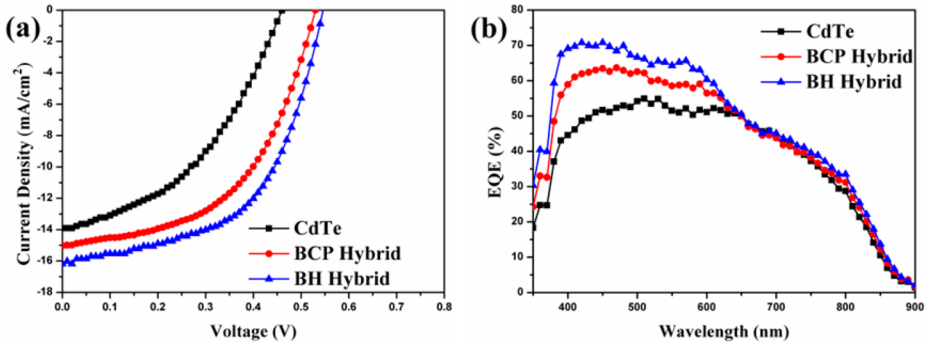

Figure 4. (a) J–V curves and (b) external quantum efficiency curves of the solar cells fabricated with different materials.

Table 2. Summary of the Carrier Mobility Based on Measurement of the SCLC Devices[a]

composition	hole mobility ($\times 10^{-4}$ cm^2/V·s)	electron mobility ($\times 10^{-4}$ cm^2/V·s)
CdTe	1.5 ± 0.2	2.6 ± 0.5
BCP hybrid	7.8 ± 0.6	3.1 ± 0.4
BH hybrid	14.4 ± 1.1	6.5 ± 0.6

[a]Note: data presented as mean ± standard deviation.

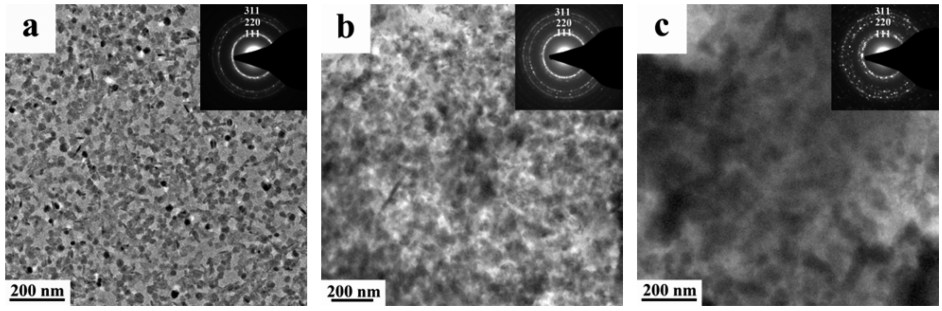

Figure 5. TEM images of the film morphology of (a) pure CdTe NCs, (b) BCP hybrid, and (c) BH hybrid after annealing at 300 °C for 15 min. The insets are corresponding electron diffraction patterns which confirm the crystalline nature of CdTe NCs.

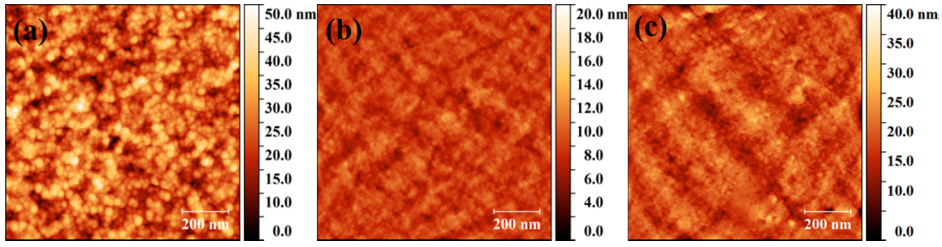

Figure 6. AFM topological images of (a) pure CdTe NCs, (b) the BCP hybrid, and (c) BH hybrid films after annealing. The rms roughness is (a) 5.9, (b) 2.1, and (c) 3.2 nm.

integration of the EQE for NC-only, BCP hybrid, and BH hybrid solar cells are 14.0, 15.2, and 16.2 mA/cm^2, respectively, which agree well with those measured from J–V curves (Table 1).[41,42] The increase in EQE in the above region in the BH hybrid solar cells can be partly attributed to the increased light absorption of the film in this region from the increased P3HT content, which is supported by the UV–vis absorption spectra (Figure S12).

In addition to increased light absorption, we hypothesized that the increase in J_{sc} and FF was due to improved carrier mobility in the hybrid materials compared to that in CdTe NCs. This was supported by the measurement of carrier

DOI: 10.1021/acsami.7b03074
ACS Appl. Mater. Interfaces 2017, 9, 17942–17948

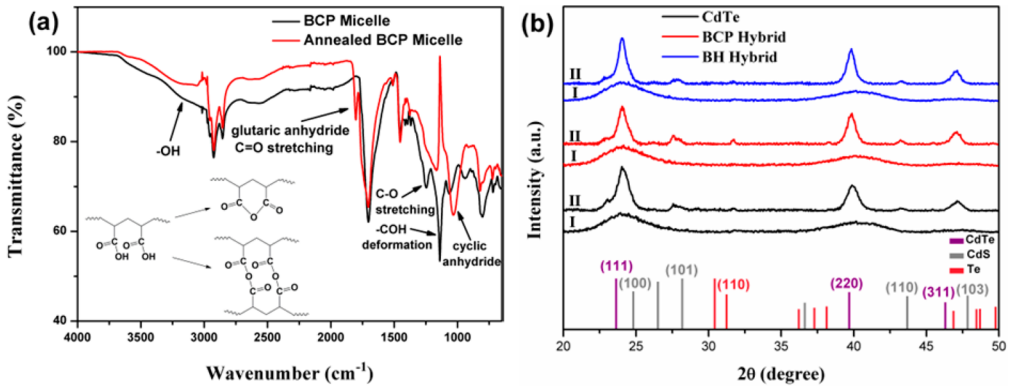

Figure 7. (a) FTIR-ATR spectra of BCP micelles and (b) XRD patterns of pure CdTe NCs and hybrid materials before (I) and after (II) annealing at 300 °C for 15 min.

mobility of the related devices through the space-charge-limited-current (SCLC) method.[43] The SCLC data (Table 2) show that the introduction of micelles increases the carrier mobility, which facilitates the charge transport and thus improved J_{sc} and FF.[44] Interestingly, the charge mobility of devices made from the BH hybrid containing an appropriate amount of homo-P3HT was greater than that of devices made from the BCP hybrid (Table 2 and Figure S13). This improved mobility led us to consider the morphological effect of the active layer and examine the film morphology.

2.4. Morphology of the Active Layer Films. The morphology of the annealed hybrid films is an important factor affecting device performance. To probe the microscopic change induced by the polymeric micelles, TEM (Figure 5) and atomic force microscopy (AFM) (Figure 6) were employed to study the active layer.

For pure CdTe NC solar cells, the nanocrystals were initially spherical or elliptical with a mean diameter of 5 nm (Figure S8), which increased to 20 nm upon annealing (Figure 5a). Others have observed the growth of CdTe through dynamic coalescence in poly(1,4-phenylenevinylene) (PPV):CdTe hybrid films upon annealing.[45] AFM (Figure 6a) shows that there are still some voids among the NCs, which likely lead to low FF and V_{oc} in the devices made from pure NCs.[46,47]

When the BCP hybrid is used, the voids between the grown NCs are reduced, as shown by the AFM (Figure 6b), as a result of the melted polymer micelles filling in the gaps. This coincides with the increase in R_{sh} (Table 1) and decrease in leakage current (Figure S14).[17] The introduction of micelles into hybrid materials thus allows one to suppress recombination loss and thereby improve the V_{oc}.[41,48]

When the BH hybrid is used, the NCs seem to grow into larger aggregates compared to those within the BCP hybrid, as shown in the extended darker regions in the TEM image (Figure 5b vs 5c). We know from Figure 2b that prior to annealing, the NCs are able to assemble into long, ordered features as a result of the nanowire shaped BH micelles. Annealing then allows the NCs to coalesce into larger features compared to those in the BCP hybrid film. Instead of the inefficient charge transport via hopping from NC to NC in pure CdTe NCs, the larger aggregates of NCs within the BH hybrid active layer facilitate the formation of a continuous pathway for electron transport[49] as supported by the SCLC data (Table 2). As seen in AFM images (Figures 6b and c), the surface of the BH hybrid film has no distinct characteristic, which is similar to that of BCP hybrid and can be attributed to the penetration of polymer into the voids among the NCs as explained above. However, the surface of the BH hybrid film appears rougher compared to that of BCP hybrid (rms roughness: 3.2 nm vs 2.1 nm). We attribute this to the increased aggregate size of NCs and to the presence of the P3HT homopolymer, which drives greater phase segregation upon annealing. This greater phase segregation likely contributes to an increase in both hole and electron mobility as observed in Table 2.

We were intrigued by the greater PCE shown by the BH hybrid-based devices compared to that of the BCP hybrid-based devices despite the greater degree of phase segregation. If the phase segregation were to become too large, the PCE is expected to decrease because of the limited exciton diffusion lengths seen in π-conjugated semiconducting polymers. We hypothesized that extensive phase segregation beyond the exciton diffusion length could be limited by the inter- and intramicellar cross-linking of PAA chains during the annealing process.

To gain insight into this, the change of chemical structure of PAA chains was investigated with FTIR-ATR spectroscopy (Figure 7a). From the FTIR-ATR spectra, it was found that the intensity of C−O bond is dramatically weakened due to the dehydration−condensation of carboxylic acid groups within PAA chains. The formation of anhydrides among interchain or intrachain carboxylic acid groups is also confirmed by the new peaks corresponding to the C═O bond stretching in cyclic or glutaric anhydrides. This dehydration−condensation reaction is also supported by thermogravimetric analysis (TGA) of the block copolymer, which shows a reduction in mass corresponding to the loss of water (Figure S15). It is important to note that the transformation of the molecular structure of PAA chains does not affect the inner crystal structure (mainly zinc blende structure) of CdTe NCs, which is demonstrated by the similarity of the XRD patterns of hybrid materials after annealing (Figure 7b). The initial diffraction peaks are generally broad and become narrower after annealing, indicating an increase in the average crystallite size. Meanwhile, the average crystallite sizes of grown NCs according to the XRD patterns reveal that the cases of the BCP hybrid (13.2 nm) and BH hybrid (14.3 nm) are larger than that in the pure CdTe NCs (10.2 nm) (Table S2), which is consistent with the nanostructure shown in TEM. It is also important to note that the XRD measurement estimates the crystallite size but not the aggregate size, which may be made up of several different crystallites.

DOI: 10.1021/acsami.7b03074
ACS Appl. Mater. Interfaces 2017, 9, 17942−17948

3. CONCLUSION

In summary, we successfully synthesized P3HT-containing ABCPs, homo-P3HT, and water-soluble CdTe NCs; fabricated HSCs from these materials; and then studied the morphology. Due to the chemical difference between conjugated P3HT block and hydrophilic PAA block, ABCPs self-assemble into spherical or cylindrical micelles in water which then transform to nanowires by comicellization with homo-P3HT additives. The BCP micelles and BH micelles presented in this work were applied in the fabrication of aqueous-processed HSCs together with CdTe NCs. Compared to the NC-only solar cells, the introduction of BCP micelles into the hybrid material dramatically increased the carrier mobility and eliminated pinholes in the film, improving the performance of HSCs. Meanwhile the addition of homo-P3HT increased the content of semiconducting polymer in BH micelles compared to ABCPs in BCP micelles and improved light absorption and charge carrier mobility of the hybrid materials. The HSCs fabricated by using hybrid materials containing BH micelles and CdTe NCs exhibits a maximum power efficiency of 4.8%. Aqueous-processed HSCs based on the ABCPs and NCs provide a facile and feasible protocol to fabricate efficient solar cells in a clean and low-cost way. We anticipate that the annealing temperature and time for aqueous-processed HSCs can be further reduced by applying other possible highly efficient materials in future work.

■ ASSOCIATED CONTENT

Supporting Information

The Supporting Information is available free of charge on the ACS Publications website at DOI: 10.1021/acsami.7b03074.

Experimental details and characterization, including additional ^{1}H NMR, GPC, MALDI-TOF, TEM, DLS, FTIR-ATR, UPS, UV−vis, DSC, TGA, XRD data, and device performance under different conditions (PDF)

■ AUTHOR INFORMATION

Corresponding Authors

*E-mail: xujt@zju.edu.cn.
*E-mail: luscombe@uw.edu.

ORCID

Jun-Ting Xu: 0000-0002-7788-9026
Christine K. Luscombe: 0000-0001-7456-1343

Notes

The authors declare no competing financial interest.

■ ACKNOWLEDGMENTS

This work was supported by National Natural Science Foundation of China (Grant 21574116) and NSF CHE-1506209. J.H.L. thanks the China Scholarship Council for financial support. J.H.L. also thanks Trevor R. Martin, Jason A. Lee, Viktoria Pakhnyuk, Jonathan Onorato, and Lauren J. Kang for their suggestions on experiment and paper revision.

■ ABBREVIATIONS

HSCs, hybrid solar cells
ABCPs, amphiphilic block copolymers
CdTe NCs, cadmium telluride nanocrystals
WCPs, water-soluble conjugated polymers
BCP, block copolymer
BH, block copolymer/homopolymer
PCE, power conversion efficiency
J_{sc}, short-circuit current density
V_{oc}, open circuit voltage
FF, fill factor
R_{sh}, shunt resistance
R_s, series resistance
SCLC, space-charge-limited-current

■ REFERENCES

(1) Wei, H. T.; Zhang, H.; Sun, H. Z.; Yang, B. Preparation of Polymer−Nanocrystals Hybrid Solar Cells through Aqueous Approaches. *Nano Today* **2012**, *7*, 316−326.
(2) Yu, W. L.; Zhang, H.; Fan, Z. X.; Zhang, J. H.; Wei, H. T.; Zhou, D.; Xu, B.; Li, F. H.; Tian, W. J.; Yang, B. Efficient Polymer/Nanocrystal Hybrid Solar Cells Fabricated from Aqueous Materials. *Energy Environ. Sci.* **2011**, *4*, 2831−2834.
(3) Bella, F.; Gerbaldi, C.; Barolo, C.; Gratzel, M. Aqueous Dye-Sensitized Solar Cells. *Chem. Soc. Rev.* **2015**, *44*, 3431−3473.
(4) Duan, C. H.; Zhang, K.; Zhong, C. M.; Huang, F.; Cao, Y. Recent Advances in Water/Alcohol-Soluble Pai-Conjugated Materials: New Materials and Growing Applications in Solar Cells. *Chem. Soc. Rev.* **2013**, *42*, 9071−9104.
(5) Wei, H. T.; Zhang, H.; Jin, G.; Na, T. Y.; Zhang, G. Y.; Zhang, X.; Wang, Y.; Sun, H. Z.; Tian, W. J.; Yang, B. Coordinatable and High Charge-Carrier-Mobility Water-Soluble Conjugated Copolymers for Effective Aqueous-Processed Polymer-Nanocrystal Hybrid Solar Cells and OFET Applications. *Adv. Funct. Mater.* **2013**, *23*, 4035−4042.
(6) Wei, H. T.; Jin, G.; Wang, L.; Hao, L.; Na, T. Y.; Wang, Y.; Tian, W. J.; Sun, H. Z.; Zhang, H. X.; Wang, H. Y.; Zhang, H.; Yang, B. Synthesis of a Water-Soluble Conjugated Polymer Based on Thiophene for an Aqueous-Processed Hybrid Photovoltaic and Photodetector Device. *Adv. Mater.* **2014**, *26*, 3655−3661.
(7) Jin, G.; Wei, H. T.; Na, T. Y.; Sun, H. Z.; Zhang, H.; Yang, B. High-Efficiency Aqueous-Processed Hybrid Solar Cells with an Enormous Herschel Infrared Contribution. *ACS Appl. Mater. Interfaces* **2014**, *6*, 8606−8612.
(8) Lee, S. H.; Kömürlü, S.; Zhao, X.; Jiang, H.; Moriena, G.; Kleiman, V. D.; Schanze, K. S. Water-Soluble Conjugated Polyelectrolytes with Branched Polyionic Side Chains. *Macromolecules* **2011**, *44*, 4742−4751.
(9) Wang, L.; Wang, H. Y.; Wei, H. T.; Zhang, H.; Chen, Q. D.; Xu, H. L.; Han, W.; Yang, B.; Sun, H. B. Unraveling Charge Separation and Transport Mechanisms in Aqueous-Processed Polymer/CdTe Nanocrystal Hybrid Solar Cells. *Adv. Energy Mater.* **2014**, *4*, 1301882.
(10) Morgenstern, F. S. F.; Rao, A.; Böhm, M. L.; Kist, R. J. P.; Vaynzof, Y.; Greenham, N. C. Ultrafast Charge- and Energy-Transfer Dynamics in Conjugated Polymer: Cadmium Selenide Nanocrystal Blends. *ACS Nano* **2014**, *8*, 1647−1654.
(11) He, Z. C.; Zhong, C. M.; Huang, X.; Wong, W. Y.; Wu, H. B.; Chen, L. W.; Su, S. J.; Cao, Y. Simultaneous Enhancement of Open-Circuit Voltage, Short-Circuit Current Density, and Fill Factor in Polymer Solar Cells. *Adv. Mater.* **2011**, *23*, 4636−4643.
(12) Thalluri, G. K. V. V; Bolsée, J. C.; Gadisa, A.; Parchine, M.; Boonen, T.; D'Haen, J.; Boyukbayram, A. E.; Vandenbergh, J.; Cleij, T. J.; Lutsen, L.; Vanderzande, D.; Manca, J. Opto-Electrical and Morphological Characterization of Water Soluble Conjugated Polymers for Eco-Friendly Hybrid Solar Cells. *Sol. Energy Mater. Sol. Cells* **2011**, *95*, 3262−3268.
(13) Qiao, Q. Q.; McLeskey, J. T. Water-Soluble Polythiophene/Nanocrystalline TiO_2 Solar Cells. *Appl. Phys. Lett.* **2005**, *86*, 153501.
(14) Cai, W. Z.; Zhong, C. M.; Duan, C. H.; Hu, Z. C.; Dong, S.; Cao, D. R.; Lei, M.; Huang, F.; Cao, Y. The Influence of Amino Group on PCDTBT-Based and P3HT-Based Polymer Solar Cells: Hole Trapping Processes. *Appl. Phys. Lett.* **2015**, *106*, 233302.
(15) Duan, C. H.; Cai, W. Z.; Hsu, B. B. Y.; Zhong, C. M.; Zhang, K.; Liu, C. C.; Hu, Z. C.; Huang, F.; Bazan, G. C.; Heeger, A. J.; Cao, Y. Toward Green Solvent Processable Photovoltaic Materials for Polymer Solar Cells: The Role of Highly Polar Pendant Groups in Charge

Carrier Transport and Photovoltaic Behavior. *Energy Environ. Sci.* **2013**, *6*, 3022−3034.
(16) Chen, Z. L.; Zhang, H.; Du, X. H.; Cheng, X.; Chen, X. G.; Jiang, Y. Y.; Yang, B. From Planar-Heterojunction to N-I Structure: An Efficient Strategy to Improve Short-Circuit Current and Power Conversion Efficiency of Aqueous-Solution-Processed Hybrid Solar Cells. *Energy Environ. Sci.* **2013**, *6*, 1597−1603.
(17) Liu, F. Y.; Chen, Z. L.; Du, X. H.; Zeng, Q. S.; Ji, T. J.; Cheng, Z. K.; Jin, G.; Yang, B. High Efficiency Aqueous-Processed MEH-PPV/CdTe Hybrid Solar Cells with a PCE of 4.20%. *J. Mater. Chem. A* **2016**, *4*, 1105−1111.
(18) Andersen, T. R.; Larsen-Olsen, T. T.; Andreasen, B.; Böttiger, A. P. L.; Carlé, J. E.; Helgesen, M.; Bundgaard, E.; Norrman, K.; Andreasen, J. W.; Jørgensen, M.; Krebs, F. C. Aqueous Processing of Low-Band-Gap Polymer Solar Cells Using Roll-to-Roll Methods. *ACS Nano* **2011**, *5*, 4188−4196.
(19) Kietzke, T.; Neher, D.; Landfester, K.; Montenegro, R.; Güntner, R.; Scherf, U. Novel Approaches to Polymer Blends Based on Polymer Nanoparticles. *Nat. Mater.* **2003**, *2*, 408−412.
(20) Yao, S. Y.; Chen, Z. L.; Li, F. H.; Xu, B.; Song, J. X.; Yan, L. L.; Jin, G.; Wen, S. P.; Wang, C.; Yang, B.; Tian, W. J. High-Efficiency Aqueous-Solution-Processed Hybrid Solar Cells Based on P3HT Dots and CdTe Nanocrystals. *ACS Appl. Mater. Interfaces* **2015**, *7*, 7146−7152.
(21) Kelley, E. G.; Albert, J. N. L.; Sullivan, M. O.; Epps, T. H., III Stimuli-Responsive Copolymer Solution and Surface Assemblies for Biomedical Applications. *Chem. Soc. Rev.* **2013**, *42*, 7057−7071.
(22) Ge, Z. S.; Liu, S. Y. Functional Block Copolymer Assemblies Responsive to Tumor and Intracellular Microenvironments for Site-Specific Drug Delivery and Enhanced Imaging Performance. *Chem. Soc. Rev.* **2013**, *42*, 7289−7325.
(23) Stefik, M.; Guldin, S.; Vignolini, S.; Wiesner, U.; Steiner, U. Block Copolymer Self-Assembly for Nanophotonics. *Chem. Soc. Rev.* **2015**, *44*, 5076−5091.
(24) Zhang, J.; Chen, X. F.; Wei, H. B.; Wan, X. H. Tunable Assembly of Amphiphilic Rod-Coil Block Copolymers in Solution. *Chem. Soc. Rev.* **2013**, *42*, 9127−9154.
(25) Schacher, F. H.; Rupar, P. A.; Manners, I. Functional Block Copolymers: Nanostructured Materials with Emerging Applications. *Angew. Chem., Int. Ed.* **2012**, *51*, 7898−7921.
(26) Tong, Z. Z.; Li, Y. M.; Xu, H. A.; Chen, H.; Yu, W. J.; Zhuo, W. Q.; Zhang, R. K.; Jiang, G. H. Corona Liquid Crystalline Order Helps to Form Single Crystals When Self-Assembly Takes Place in the Crystalline/Liquid Crystalline Block Copolymers. *ACS Macro Lett.* **2016**, *5*, 867−872.
(27) Fetsch, C.; Gaitzsch, J.; Messager, L.; Battaglia, G.; Luxenhofer, R. Self-Assembly of Amphiphilic Block Copolypeptoids − Micelles, Worms and Polymersomes. *Sci. Rep.* **2016**, *6*, 33491.
(28) He, W. N.; Xu, J. T. Crystallization Assisted Self-Assembly of Semicrystalline Block Copolymers. *Prog. Polym. Sci.* **2012**, *37*, 1350−1400.
(29) Yang, J. X.; Fan, B.; Li, J. H.; Xu, J. T.; Du, B. Y.; Fan, Z. Q. Hydrogen-Bonding-Mediated Fragmentation and Reversible Self-Assembly of Crystalline Micelles of Block Copolymer. *Macromolecules* **2016**, *49*, 367−372.
(30) Mohd Yusoff, S. F.; Gilroy, J. B.; Cambridge, G.; Winnik, M. A.; Manners, I. End-to-End Coupling and Network Formation Behavior of Cylindrical Block Copolymer Micelles with a Crystalline Polyferrocenylsilane Core. *J. Am. Chem. Soc.* **2011**, *133*, 11220−11230.
(31) Rizis, G.; van de Ven, T. G. M.; Eisenberg, A. Homopolymers as Structure-Driving Agents in Semicrystalline Block Copolymer Micelles. *ACS Nano* **2015**, *9*, 3627−3640.
(32) Fan, B.; Wang, R. Y.; Wang, X. Y.; Xu, J. T.; Du, B. Y.; Fan, Z. Q. Crystallization-Driven Co-Assembly of Micrometric Polymer Hybrid Single Crystals and Nanometric Crystalline Micelles. *Macromolecules* **2017**, *50*, 2006−2015.
(33) Jeffries-El, M.; Sauvé, G.; McCullough, R. D. In-Situ End-Group Functionalization of Regioregular Poly(3-alkylthiophene) Using the Grignard Metathesis Polymerization Method. *Adv. Mater.* **2004**, *16*, 1017−1019.
(34) Gilroy, J. B.; Lunn, D. J.; Patra, S. K.; Whittell, G. R.; Winnik, M. A.; Manners, I. Fiber-Like Micelles via the Crystallization-Driven Solution Self-Assembly of Poly(3-hexylthiophene)-*b*-Poly(methyl methacrylate) Copolymers. *Macromolecules* **2012**, *45*, 5806−5815.
(35) Cui, H. G.; Chen, Z. Y.; Zhong, S.; Wooley, K. L.; Pochan, D. J. Block Copolymer Assembly via Kinetic Control. *Science* **2007**, *317*, 647−650.
(36) Fan, B.; Liu, L.; Li, J. H.; Ke, X. X.; Xu, J. T.; Du, B. Y.; Fan, Z. Q. Crystallization-Driven One-Dimensional Self-Assembly of Polyethylene-*b*-Poly(*tert*-butylacrylate) Diblock Copolymers in DMF: Effects of Crystallization Temperature and the Corona-Forming Block. *Soft Matter* **2016**, *12*, 67−76.
(37) Du, Z. X.; Xu, J. T.; Fan, Z. Q. Micellar Morphologies of Poly(ε-caprolactone)-*b*-Poly(ethylene oxide) Block Copolymers in Water with a Crystalline Core. *Macromolecules* **2007**, *40*, 7633−7637.
(38) Burrows, N. D.; Penn, R. L. Cryogenic Transmission Electron Microscopy: Aqueous Suspensions of Nanoscale Objects. *Microsc. Microanal.* **2013**, *19*, 1542−1553.
(39) Chen, H. C.; Lai, C. W.; Wu, I. C.; Pan, H. R.; Chen, I. W. P.; Peng, Y. K.; Liu, C. L.; Chen, C.; Chou, P. T. Enhanced Performance and Air Stability of 3.2% Hybrid Solar Cells: How the Functional Polymer and CdTe Nanostructure Boost the Solar Cell Efficiency. *Adv. Mater.* **2011**, *23*, 5451−5455.
(40) Sun, C.; Wu, Z. H.; Yip, H. L.; Zhang, H.; Jiang, X. F.; Xue, Q. F.; Hu, Z. C.; Hu, Z. H.; Shen, Y.; Wang, M. K.; Huang, F.; Cao, Y. Amino-Functionalized Conjugated Polymer as an Efficient Electron Transport Layer for High-Performance Planar-Heterojunction Perovskite Solar Cells. *Adv. Energy Mater.* **2016**, *6*, 1501534.
(41) Zhao, Y.; Zeng, Q. S.; Liu, X.; Jiao, S. H.; Pang, G. S.; Du, X. H.; Zhang, K.; Yang, B. Highly Efficient Aqueous-Processed Polymer/Nanocrystal Hybrid Solar Cells with an Aqueous-Processed TiO2 Electron Extraction Layer. *J. Mater. Chem. A* **2016**, *4*, 11738−11746.
(42) Wang, M.; Cai, D. D.; Yin, Z. G.; Chen, S. C.; Du, C. F.; Zheng, Q. D. Asymmetric-Indenothiophene-Based Copolymers for Bulk Heterojunction Solar Cells with 9.14% Efficiency. *Adv. Mater.* **2016**, *28*, 3359−3365.
(43) Chen, Z. L.; Liu, F. Y.; Zeng, Q. S.; Cheng, Z. K.; Du, X. H.; Jin, G.; Zhang, H.; Yang, B. Efficient Aqueous-Processed Hybrid Solar Cells from a Polymer with a Wide Bandgap. *J. Mater. Chem. A* **2015**, *3*, 10969−10975.
(44) Holliday, S.; Ashraf, R. S.; Wadsworth, A.; Baran, D.; Yousaf, S. A.; Nielsen, C. B.; Tan, C.; Dimitrov, S. D.; Shang, Z.; Gasparini, N.; Alamoudi, M.; Laquai, F.; Brabec, C. J.; Salleo, A.; Durrant, J. R.; McCulloch, I. High-Efficiency and Air-Stable P3HT-Based Polymer Solar Cells with a New Non-Fullerene Acceptor. *Nat. Commun.* **2016**, *7*, 11585.
(45) Yu, W. L.; Zhang, H.; Tian, H. R.; Wei, H. T.; Liu, W. X.; Zhu, J.; Zhang, J. H.; Yang, B. Correlation between Annealing-Induced Growth of Nanocrystals and the Performance of Polymer: Nanocrystals Hybrid Solar Cells. *J. Phys. Chem. C* **2012**, *116*, 1322−1328.
(46) Crisp, R. W.; Panthani, M. G.; Rance, W. L.; Duenow, J. N.; Parilla, P. A.; Callahan, R.; Dabney, M. S.; Berry, J. J.; Talapin, D. V.; Luther, J. M. Nanocrystal Grain Growth and Device Architectures for High-Efficiency CdTe Ink-Based Photovoltaics. *ACS Nano* **2014**, *8*, 9063−9072.
(47) Jin, G.; Chen, Z. L.; Dong, C. W.; Cheng, Z. K.; Du, X. H.; Zeng, Q. S.; Liu, F. Y.; Sun, H. Z.; Zhang, H.; Yang, B. Aqueous-Processed Insulating Polymer/Nanocrystal Hybrid Solar Cells. *ACS Appl. Mater. Interfaces* **2016**, *8*, 7101−7110.
(48) Du, X. H.; Chen, Z. L.; Liu, F. Y.; Zeng, Q. S.; Jin, G.; Li, F. H.; Yao, D.; Yang, B. Improvement in Open-Circuit Voltage of Thin Film Solar Cells from Aqueous Nanocrystals by Interface Engineering. *ACS Appl. Mater. Interfaces* **2016**, *8*, 900−907.
(49) Huynh, W. U.; Dittmer, J. J.; Alivisatos, A. P. Hybrid Nanorod-Polymer Solar Cells. *Science* **2002**, *295*, 2425−2427.

DOI: 10.1021/acsami.7b03074
ACS Appl. Mater. Interfaces 2017, 9, 17942−17948